Neuronal activity disrupts myelinated axon integrity in the absence of NKCC1b

Neuronal activity disrupts myelinated axon integrity in the absence of NKCC1b

Katy LH Marshall-Phelps[1,^], Linde Kegel[1,^], Marion Baraban[1], Torben Ruhwedel[2], Rafael G Almeida[1], Maria Rubio-Brotons[1], Anna Klingseisen[1], Silvia Benito-Kwiecinski[1], Jason J Early[1], Jenea M Bin[1], Daumante Suminaite[1], Matthew R Livesey[1], Wiebke Möbius[2], Richard J Poole[3] and David A Lyons[1,*].

1. Centre for Discovery Brain Sciences, University of Edinburgh, Edinburgh EH16 4SB, UK.

2. Electron Microscopy Core Unit, Department of Neurogenetics, Max-Planck-Institute of Experimental Medicine, Hermann-Rein-Str. 3, D-37075 Göttingen, Germany

3. Department of Cell and Developmental Biology, University College London, London WC1E 6BT, UK.

^. These authors contributed equally to this work.
*. Corresponding author: david.lyons@ed.ac.uk

Running title: Myelinated axon integrity requires NKCC1b

Abstract

Through a genetic screen in zebrafish, we identified a mutant with disruption to myelin in both the CNS and PNS, caused by a mutation in a previously uncharacterized gene, *slc12a2b,* predicted to encode a Na^+, K^+, and Cl^- (NKCC) co-transporter, NKCC1b. *slc12a2b/*NKCC1b mutants exhibited a severe and progressive pathology in the PNS, characterized by dysmyelination and swelling of the periaxonal space at the axon-myelin interface. Cell-type specific loss of *slc12a2b/*NKCC1b in either neurons or myelinating Schwann cells recapitulated these pathologies. Given that NKCC1 is critical for ion homeostasis, we asked whether the disruption to myelinated axons in *slc12a2b/*NKCC1b mutants is affected by neuronal activity. Strikingly, we found that blocking neuronal activity completely prevented and could even rescue the pathology in *slc12a2b/*NKCC1b mutants. Together our data indicate that NKCC1b is required to maintain neuronal activity-related solute homeostasis and the integrity of myelinated axons.

Introduction

Interactions between axons and myelinating glia (Schwann cells in the PNS and oligodendrocytes in the central nervous system, CNS) underpin many aspects of nervous system formation, health and function. The myelination of axons has long been known to facilitate rapid saltatory conduction, due to the multi-lamellar wrapping of myelin sheaths around axons and the sequestration of distinct ion channels to discrete domains along the myelinated axon, including voltage-gated sodium channels to nodes of Ranvier. Recently, however, it has become clear that the physiology of myelinated axons is more complex than previously thought. For example, it has been proposed that electrical conduction through the periaxonal space between the axon and the overlying myelin sheath also contributes to the fundamental nature of conduction along myelinated axons (Cohen et al., 2020). Indeed, numerous ion channels, transporters and neurotransmitter receptors are present at the axon-myelin interface, and are thus well placed to regulate myelinated axon physiology, structure and integrity (Suminaite et al., 2019). These include axonal ion channels that extrude ions into the periaxonal space upon neuronal activity and channels in the juxtaposed myelin sheath that buffer ions from the periaxonal space (Rash et al., 2016; Wang et al., 1993; Schirmer et al., 2018; Larson et al., 2018). In addition, monocarboxylate transporters juxtaposed at the axon-myelin interface are thought to mediate the transfer of metabolic substrates from the myelinating oligodendrocyte to the axon through the periaxonal space (Saab et al., 2016; Fünfschilling et al., 2012). Furthermore, receptors for neurotransmitters, neuromodulators and neuropeptides are localised to the axon-myelin interface (Saab et al., 2016; Micu et al., 2018; 2016) and have been proposed to mediate adaptations to myelin structure in response to neuronal activity that may even fine-tune neural circuit function (Almeida and Lyons, 2017; Monje, 2018; Fields, 2015).

The importance of physiological interactions between axons and myelinating glia at the axon-myelin interface is only now becoming clear, with dysregulation implicated in susceptibility to seizures (Larson et al., 2018) and neuronal health (Schirmer et al., 2018; Saab et al., 2016; Lee et al., 2012; Jha et al., 2019), and potentially also neurodevelopmental, neuropsychiatric and neurodegenerative disorders (Micu et al., 2018; Gibson et al., 2018; Stassart et al., 2018). To gain deeper insight into myelinated axon biology, we executed a gene discovery screen in zebrafish, through which we identified a mutant with severe disruption to myelin. This phenotype was caused by a mutation in a previously uncharacterised zebrafish gene, *slc12a2b*, predicted to encode a sodium (Na^+), potassium (K^+), and chloride (Cl^-) co-transporter, NKCC1b. NKCC1 co-transports Na^+, K^+ and Cl^- together with water, typically from the extracellular space into cells (Zeuthen and MacAulay, 2012; MacAulay and Zeuthen, 2010) and has been implicated in regulating many aspects of ion and fluid homeostasis in the healthy nervous system (Delpire et al., 1999; Flagella et al., 1999; Dixon et al., 1999; Macvicar et al., 2001; Su et al., 2002; Larsen et al., 2014; Stenesen et al., 2019). and following injury and disease (Blaesse et al., 2009; Ben-Ari, 2017; Yousuf et al., 2017; Gagnon and Delpire, 2013). Here we show that NKCC1b is required to maintain the integrity of myelinated axons following neuronal activity, implicating it as a key regulator of solute homeostasis at the axon-myelin interface.

Results and Discussion

Mutation of zebrafish slc12a2b disrupts myelination

To help elucidate mechanisms underpinning myelinated axon formation, health and function, we carried out an ENU mutagenesis-based gene discovery screen using zebrafish ((Kegel et al., 2019; Klingseisen et al., 2019) and **Methods**). To assess myelin, we used the transgenic reporter Tg(mbp:EGFP-CAAX) in which green fluorescent protein is targeted to the membrane of myelinating glia (Almeida et al., 2011). One of the mutant alleles that we identified, *ue58*, exhibited a striking phenotype, whereby myelin was disrupted in both the PNS and CNS (**Figure 1A** and (Moyon et al., 2019)). Although CNS pathology was evident in *ue58* mutants, disruption to myelin in the PNS was more prominent and emerged earlier. We found that myelin made by Schwann cells along the posterior lateral line nerve (pLLn) was particularly disrupted (**Figure 1B+C**). In addition, differential interference contrast (DIC) imaging of *ue58* mutants revealed extensive oedema (excess fluid) along the entire length of the pLLn of all mutants (**Figure 1D**). Time-course analyses of myelin indicated that myelin sheaths appear to form relatively normally by 3 days post-fertilisation (dpf) in *ue58* mutants, but become progressively disrupted from 4dpf onwards (**Supplementary Figure 1).** Despite the severe derangement of myelin and extensive nerve oedema, we observed no other overt disruption to the development of *ue58* homozygous mutants (**Figure 1E**), which are, in fact, viable.

To identify the mutation responsible for the *ue58* phenotype, we performed whole genome sequencing of mutant larvae (**Methods**). This identified genetic linkage between the mutant phenotype and the start of chromosome 8 (**Supplementary Figure 2**), wherein we identified a T to A change predicted to induce a STOP codon in an open reading frame partially annotated at the time of sequence analysis (**Figure 1F and Supplementary Figure 2** and **Methods**). We identified sequence similarity between this partially annotated region and another zebrafish gene, *slc12a2* (Abbas and Whitfield, 2009), which encodes an NKCC1 co-transporter (Chew et al., 2019), to which we found no linkage of the mutant phenotype (**Supplementary Figure 2**). To further characterise the candidate gene on chromosome 8*,* we amplified mRNA based on the partially annotated sequence, and identified a product similar to that encoded by the previously defined *slc12a2* gene (**Figure 1F-I**). Alignment of this new NKCC1-like open reading frame to genomic sequence indicated that the *ue58* mutation introduced a premature STOP codon in the last exon (exon 26) of the gene (**Figure 1F**), predicted to truncate the last highly conserved 40 amino acids of the protein (**Figure 1G**).

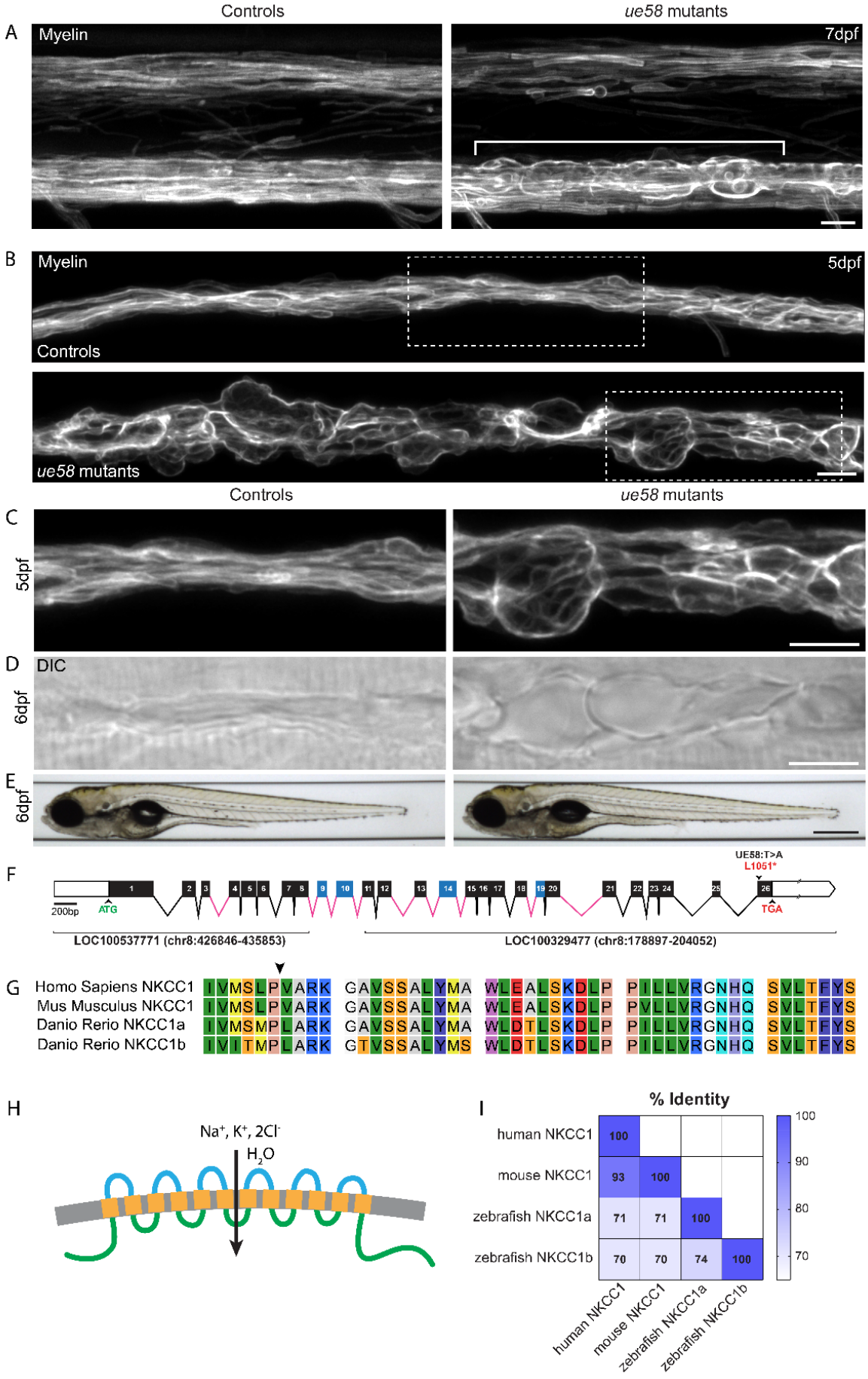
Controls
ue58 mutants
A
Myelin
7dpf
B
Myelin
5dpf
Controls
ue58 mutants
Controls
ue58 mutants
C
5dpf
D
DIC
6dpf
E
6dpf
F
UE58:T>A
L1051*
200bp
ATG
TGA
LOC100537771 (chr8:426846-435853)
LOC100329477 (chr8:178897-204052)
G
Homo Sapiens NKCC1
Mus Musculus NKCC1
Danio Rerio NKCC1a
Danio Rerio NKCC1b
H
Na+, K+, 2Cl-
H2O
I
% Identity
human NKCC1
mouse NKCC1
zebrafish NKCC1a
zebrafish NKCC1b
100
93
71
70
74
90
80
70

Figure 1. *ue58* mutant zebrafish have a severe peripheral nerve myelin pathology.
A. Confocal images of the spinal cord of Tg(mbp:EGFP-CAAX) control (left) and ue58 mutant (right) at 7dpf showing disruption to CNS myelin (region within brackets). Scale bar, 10 µm.
B. Confocal images of the pLLn in Tg(mbp:EGFP-CAAX) control (top) and *ue58* mutant (bottom) animals at 5dpf showing major disruption to myelin. Scale bar, 10 µm.
C. Higher magnification images of areas demarcated in panel B showing myelin in control (left) and *ue58* mutant (right) animals. Scale bar, 10 µm.
D. Differential Interference Contrast (DIC) images of Tg(mbp:EGFP-CAAX) control (left) and *ue58* mutants (right) at 6dpf showing appearance of tissue oedema. Scale bar, 10 µm.
E. Brightfield images of control (left) and *ue58* mutants (right) at 6dpf showing generally normal morphological development. Scale bar, 0.5 mm.
F. Genomic structure of the zebrafish *slc12a2b* gene, showing exons (boxes) and introns (lines). White boxes denote untranslated regions. Exons in black were annotated in partial genomic sequences LOC100537771 and LOC100329477 and matched homologous exons in the orthologue *slc12a2a*. Exons in blue did not align with any annotated genomic sequence and their limits were inferred by homology with *slc12a2a* genomic structure. Exons are drawn to scale relative to each other; introns in pink contain unknown bases ('N') and are of unknown size. The start (ATG) and stop (TGA) codons are indicated in green and red, respectively. The *ue58* causes a T>A mutation in exon 26 leading to a premature STOP codon.
G. Alignment of the 40 most C-terminal amino acids of NKCC1b shows high similarity between species in this domain. Arrowhead indicates the position of the premature STOP codon introduced by *ue58*.
H. Protein structural prediction algorithms, using CCTOP, indicate that NKCC1b in zebrafish is likely to have intracellular N and C termini and 12 transmembrane domains.
I. Sequence similarities of the protein products of zebrafish NKCC1a, NKCC1b and murine and human NKCC1 homologues.

Quantitative analyses of the myelin phenotype indicated that only animals homozygous for the *ue58* mutation exhibited a significant disruption to myelination, with heterozygous animals appearing similar to wildtype (**Supplementary Figure 3A-D**). To further test whether the *ue58* mutant phenotype was indeed due to disruption of this putative NKCC1-encoding gene, we injected synthetic mRNA encoding our newly isolated NKCC1-like product into *ue58* mutants, and found that this rescued their myelin defects (**Supplementary Figure 3E-F**). Given the previous incomplete annotation at the chromosome 8 mutant-linked locus harbouring the NKCC1-like sequence, we independently targeted two regions of the candidate gene using CRISPR guide RNAs. Independent targeting of exon 1 or exon 26, where our ENU-induced mutation resided, resulted in severe disruption to myelin morphology, as assessed by Tg(mbp:EGFP-CAAX) (**Supplementary Figure 4**). Together our data indicate that a novel gene encoding an NKCC1-like protein is required for the maintenance of myelin morphology, and that the C-terminus is functionally essential. Given the previous characterisation of a separate NKCC1-encoding gene (*slc12a2*) in zebrafish (Abbas and Whitfield, 2009), we designate our newly described gene as *slc12a2b* and the encoded protein as NKCC1b, and suggest that the originally annotated gene be referred to as *slc12a2a* and its encoded protein NKCC1a. The crystal structure for the zebrafish NKCC1a protein was recently solved and found similar to that of mouse and human NKCC1 (Chew et al., 2019). NKCC1a and NKCC1b have the same predicted structure (**Figure 1H**) and degree of similarity to their mouse and human NKCC1 counterparts (**Figure 1I**), which further indicates that *slc12a2b* encodes an NKCC1 co-transporter.

Disruption to NKCC1b leads to enlargement of the periaxonal space and dysmyelination
Given that NKCC1 typically co-transports ions (Na^+, K^+, $2Cl^-$) and water into cells, loss of its function would be predicted to lead to extracellular ion and water accumulation, which could account for the observed oedema and dysregulation of myelin seen in the *slc12a2b*^{ue58}

mutant. In line with this, glial-specific disruption to an orthologue of NKCC1 (Ncc69) has been shown to lead to fluid accumulation in the extracellular space of peripheral nerves in Drosophila (Leiserson et al., 2010). We have recently shown, using immuno-gold labelling of an anti-NKCC1 antibody visualised by electron microscopy that NKCC1 is localised at the axon-myelin interface in the mammalian CNS, and is present at both sides of the periaxonal space, both in the innermost layer of the myelin sheath and the juxtaposed axon itself (Moyon et al., 2019). This positions NKCC1 as a potential regulator of ion and solute homeostasis at the axon-myelin interface of vertebrate myelinated axons.

To test how NKCC1b disruption affects myelin and peripheral nerve ultrastructure, we carried out high pressure freezing-based cryopreservation of zebrafish larvae for transmission electron microscopy (TEM) (Weil et al., 2019). To increase the likelihood of optimally preserving tissue with oedema, we cryopreserved animals between 4 and 5 dpf when the phenotype first emerged. Because we carried out our TEM analyses at the onset of pathology, we observed that many axons were ensheathed by normal appearing myelin, corroborating our reporter-based time course analyses, which showed that myelin first appears to be relatively normal before pathology progresses over time. However, our TEM analyses did reveal striking oedema in the periaxonal space between axons and overlying multi-lamellar myelin sheaths in 6/8 mutant nerves examined (**Figure 2A**). In sufficiently well-preserved cases, we measured the periaxonal space between the axon and the first layer of myelin, and found that that this was substantially enlarged in mutant axons (**Figure 2B**). Oedema was always found in association with myelinated axons, and never in other regions of the nerve, including unmyelinated axon bundles, in or near Schwann cell bodies, or in neighbouring tissue. Our observations support the premise that NKCC1 regulates solute homeostasis at the axon-myelin interface.

Our TEM analysis also revealed evidence of occasional myelin outfoldings (**Supplementary Figure 5**) and a small number of abnormally large axons (**Figure 2A+C and Supplementary Figure 5**), suggesting the possibility of additional pathologies in *slc12a2* mutants. To investigate this further, we analysed transgenic reporters that allowed us to more broadly assess axonal and myelinating Schwann cell morphology. To visualise axons in the context of myelination, we imaged the double transgenic reporter Tg(cntn1b:mCherry, mbp:EGFP-CAAX) (**Figure 2D**). This showed that axons of the pLLn were defasciculated, and had localised swelling at discrete points along their length (**Figure 2D**), likely explaining the appearance of occasional enlarged axons noted by TEM. To assess Schwann cell morphology, we mosaically labelled cells using a membrane-tethered reporter (**Methods**) and observed individual mutant Schwann cells with variable levels of disruption (**Figure 2E**). While many *slc12a2b*^{ue58} mutant Schwann cells exhibited signs of significant swelling, this was accompanied by a shortening of cell length compared to controls (**Figure 2E-G**). We also observed that cells could undergo significant membrane blebbing, while others had myelin outfoldings as indicated by our TEM analysis (**Figure 2E, Supplementary Figure 5**). In some cases, we saw Schwann cells with areas of normal appearing myelin in close proximity to grossly disrupted areas (**Figure 2E)**, indicating the dynamic progressive nature of the NKCC1b loss of function pathology.

Together our observations show that disruption to NKCC1b leads to major dysregulation of the periaxonal space and the integrity of myelinated axons. It remains to be determined

whether the distinct morphological manifestations of NKCC1b loss of function all reflect dysregulation of ion and fluid homeostasis at the axon-myelin interface, or multiple distinct roles for NKCC1b in axons and/or myelinating glia.

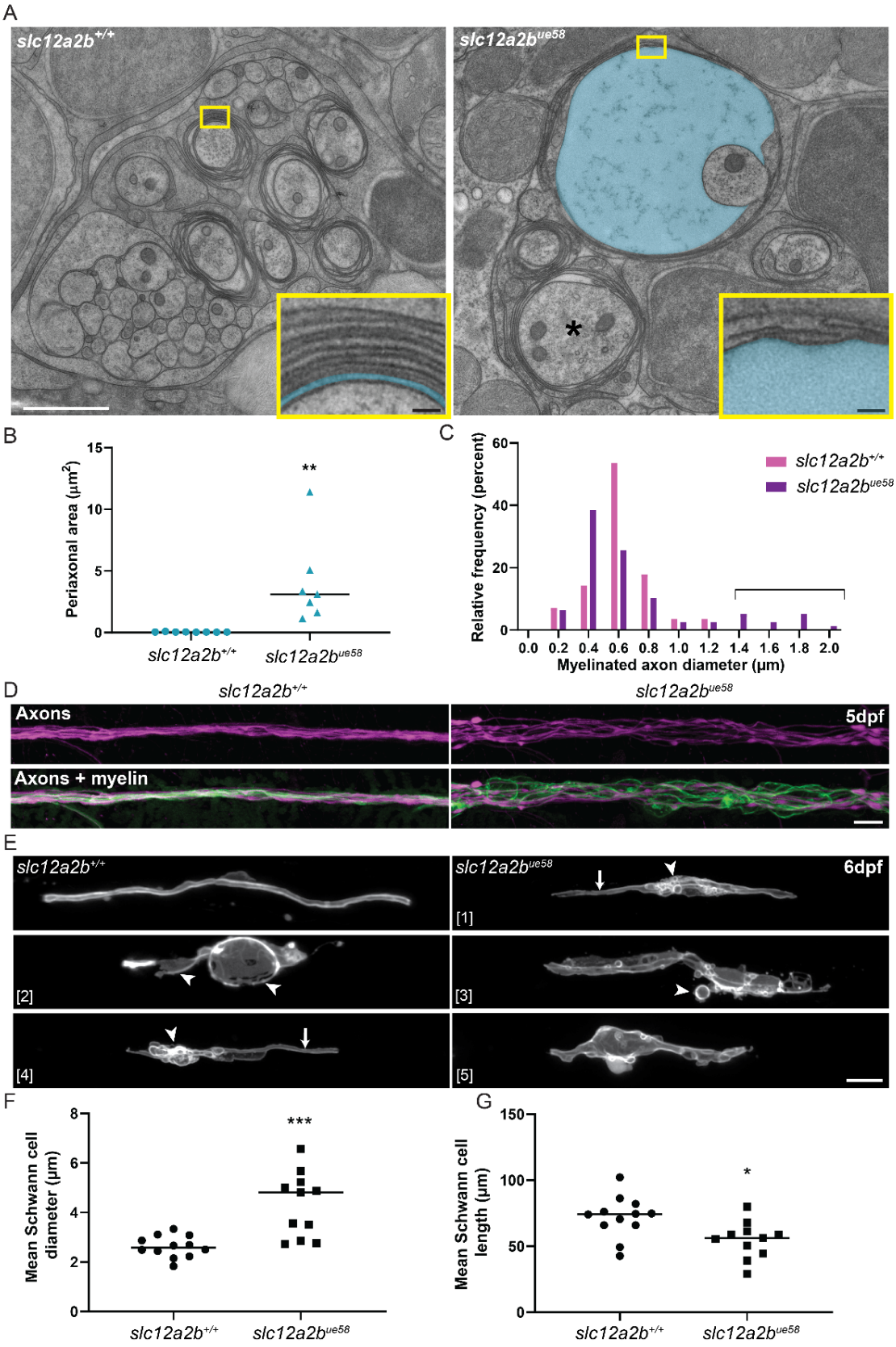

Figure 2. Disruption to NKCC1b leads to swelling of the periaxonal space, dysmyelination and axonal disorganisation.

A. Electron micrographs of high pressure frozen pLLn in control (left panel) and *slc12a2b*^{ue58} mutant (right) at 5dpf. *slc12a2b*^{ue58} mutants show significant enlargement of the periaxonal space, highlighted in blue and enlarged axons (asterisk). Insets show a higher magnification to highlight the periaxonal space in controls and *slc12a2b*^{ue58} mutants. White scale bar, 1 μm. Black scale bars, 50nm.

B. Quantification of periaxonal area in control and *slc12a2b*^{ue58} mutants (control 0.05 ± 0.02 vs *slc12a2b*^{ue58} 4 ± 3.5, p = 0.0065). Two-tailed Student's t-test was used to assess statistical significance. **p<0.01. Each point represents an individual myelinated axon from 3 control and 5 *slc12a2b*^{ue58} mutant animals.

C. Quantification of the diameter of myelinated axons in control and *slc12a2b*^{ue58} mutants. Bracket indicates axons in the mutant outwith normal diameter.

D. Confocal images of live Tg(cntn1b:mCherry), Tg(mbp:EGFP-CAAX) double transgenic control (left) and *slc12a2b*^{ue58} mutant (right) animals at 5dpf indicates axonal defasciculation and derangement of myelin. Scale bar, 10 μm.

E. Confocal images of individual mosaically labelled Schwann cells in control (top left panel) and *slc12a2b*^{ue58} mutants (panels 1-5) highlighting the variable morphological manifestation of the mutant phenotype. Scale bar, 10 μm. Arrows point to regions of normal appearing myelin and arrowheads to dysmyelination.

F. Quantitation of mean Schwann cell diameter in maximum intensity projection images of single Schwann cells at 6dpf (control 2.6 ± 0.4 vs *slc12a2b*^{ue58} 4.3 ± 1.3, p = 0.0003). Two-tailed Student's t-test was used to assess statistical significance. ***p<0.001. Each point represents a single cell from 11 control and 10 *slc12a2b*^{ue58} mutant animals. Scale bar, 10 μm.

G. Quantitation of mean Schwann cell length in maximum intensity projection images of single Schwann cells at 6dpf (control 72.1 ± 15.7 vs *slc12a2b*^{ue58} 54.7 ± 13.8, p = 0.011). Two-tailed Student's t-test was used to assess statistical significance. *p<0.05. Each point represents a single cell from 11 control and 10 *slc12a2b*^{ue58} mutant animals.

Loss of NKCC1b function in myelinating glia or neurons disrupts myelinated axon integrity

To test whether NKCC1b mediates distinct roles in myelinating Schwann cells and neurons, we undertook cell type-specific targeting approaches using CRISPR-Cas9 technology. To do so, we placed a gRNA targeting exon 1 of *slc12a2b* in a plasmid that also drove expression of the Cas9 nuclease in a cell type-specific manner. To drive expression in myelinating glia we used the myelin basic protein (mbp) gene regulatory sequence and for neurons either nefma or nbt gene regulatory sequences (**Figure 3A and Methods**). We saw the dysmyelination and oedema characteristic of *slc12a2b*^{ue58} mutants in animals in which *slc12a2b* was specifically targeted in myelinating glia (**Figure 3B+C**). Reflecting the mosaic nature of our cell type-specific targeting, the phenotype in animals with myelinating glial loss of *slc12a2b* function was observed discontinuously along the nerve. We also observed disruption to myelin morphology upon neuron-specific loss of *slc12a2b* function (**Figure 3B+C**). Reflecting the long-range axonal projections of individual neurons of the posterior lateral line ganglion (pLLg), we saw disruption to myelin along the entire length of affected nerves in animals with neuron-specific loss of *slc12a2b* function.

Together our results indicate that disruption to NKCC1b in either myelinating Schwann cells or neurons is sufficient to drive pathology, suggesting that NKCC1 functions at the axon-myelin interface in both the axon and Schwann cell to ensure myelinated axon integrity.

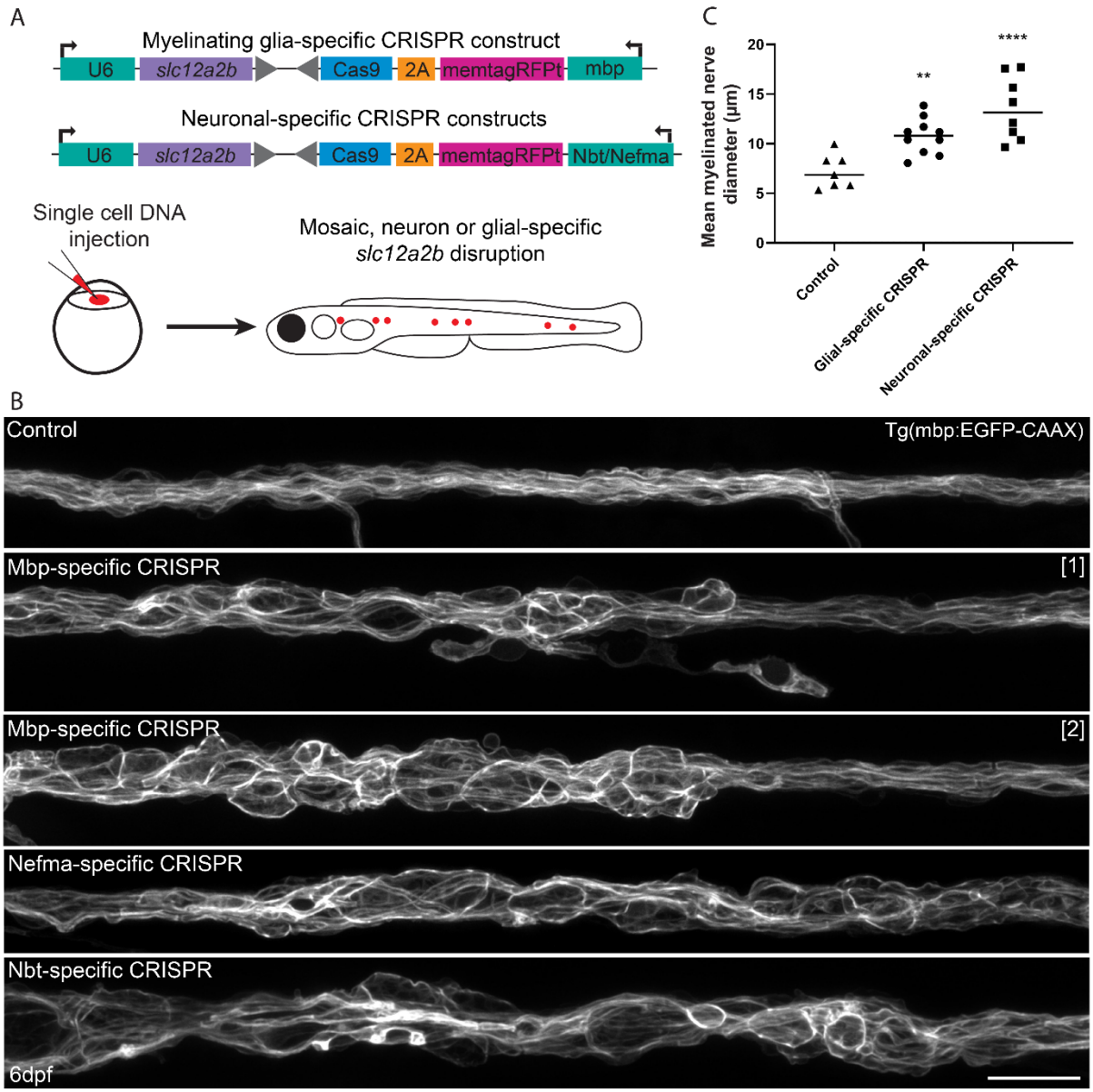

Figure 3. Cell-type specific disruption of *slc12a2b* in either neurons or Schwann cells leads to myelin pathology.
A. Schematic overviews of constructs used to induce *slc12a2b* mutations in myelinating glial cells (top) and neurons (bottom), which are separately injected into embryos at the single cell stage, leading to mosaic expression (red dots) at later stages, when myelination is examined.
B. Confocal images of Schwann cells along the pLLn in 6dpf Tg(mbp:EGFP-CAAX) control (top), two genetically mosaic animals, in which *slc12a2b* has been targeted in myelinating glial cells and two further mosaic animals in which *slc12a2b* has been targeted in neurons. Scale bar, 20 μm.
C. Quantitation of mean myelinated nerve diameter in controls compared to larvae with glial- or neuronal-specific *slc12a2b*-specific disruption at 6dpf. One-way ANOVA followed by Tukey's multiple comparison test was used to assess statistical significance. ** $p<0.01$, **** $p<0.0001$. Each point represents an individual animal.

Neuronal activity drives the myelin pathology observed in NKCC1b mutants

The fact that NKCC1 is important for ion homeostasis and that it is localised to the axon-myelin interface (Moyon et al., 2019) suggested the possibility it may have a key role in regulating ion homeostasis in myelinated axons following neuronal activity. To test this hypothesis, we inhibited neuronal activity by injecting tetrodotoxin (TTX) into the yolk of 3 dpf control and constitutive *slc12a2b*^{ue58} mutant animals to block action potential firing (**Figure 4A**). We confirmed the efficacy of TTX injections by assessing motility and only pursued analyses of fully paralysed zebrafish larvae. We found that myelin at 4 dpf was quantitatively indistinguishable between control animals and TTX-injected *slc12a2b*^{ue58} mutants, whereas sham-injected mutants exhibited their characteristic myelin pathology (**Figure 4B-C**). This indicates that the pathology seen in animals with loss of NKCC1b function is driven by neuronal activity. We next asked whether the severe disruption to myelinated axons in *slc12a2b*^{ue58} mutants might be reversible, if neuronal activity was inhibited. We found that TTX injection at 6dpf after pathology had emerged was indeed capable of partially reducing myelin disruption in *slc12a2b*^{ue58} mutants (**Figure 4D,E,G)**, indicating that ongoing neuronal activity contributes to the progression of pathology in the absence of NKCC1b. We next wanted to test whether *slc12a2b* was required specifically in myelinating glia to maintain myelin integrity in response to neuronal activity. We grew Tg(mbp:EGFP-CAAX) animals in which *slc12a2b* was disrupted in myelinating Schwann cells only to 6 dpf and screened them for the presence of myelinated axon pathology. We then injected a subset of animals exhibiting pathology with either vehicle or TTX and assessed myelination (**Figure 4D+F**). While we continued to see myelin pathology in sham-injected animals with myelinating glial-specific targeting of *slc12a2b*, we observed that pathology was significantly attenuated within hours following TTX injection (**Figure 4F+H**). This result indicates that NKCC1b is required by myelinating Schwann cells to maintain solute homeostasis following neuronal activity and maintain myelinated axon integrity.

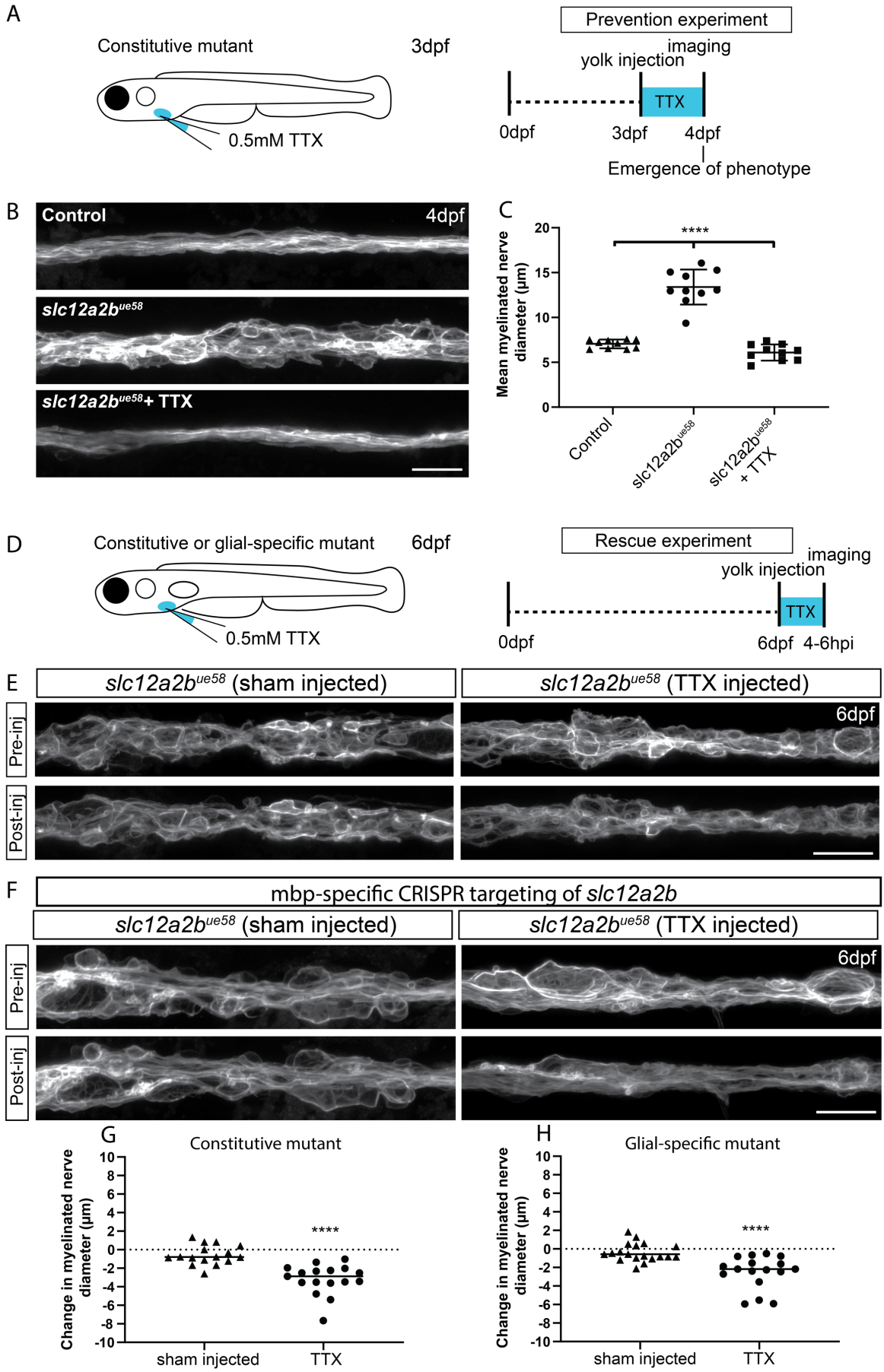
A
Constitutive mutant
3dpf
0.5mM TTX
Prevention experiment
yolk injection
imaging
TTX
0dpf
3dpf
4dpf
Emergence of phenotype
B
Control
4dpf
slc12a2b^ue58
slc12a2b^ue58+ TTX
C
Mean myelinated nerve diameter (µm)
****
Control
slc12a2b^ue58
slc12a2b^ue58 + TTX
D
Constitutive or glial-specific mutant
6dpf
0.5mM TTX
Rescue experiment
yolk injection
imaging
TTX
0dpf
6dpf 4-6hpi
E
slc12a2b^ue58 (sham injected)
slc12a2b^ue58 (TTX injected)
Pre-inj
Post-inj
6dpf
F
mbp-specific CRISPR targeting of slc12a2b
slc12a2b^ue58 (sham injected)
slc12a2b^ue58 (TTX injected)
Pre-inj
Post-inj
6dpf
G
Constitutive mutant
Change in myelinated nerve diameter (µm)
****
sham injected
TTX
H
Glial-specific mutant
Change in myelinated nerve diameter (µm)
****
sham injected
TTX

Figure 4. Neuronal activity drives peripheral nerve pathology in *slc12a2b* mutants.
A. Schematic overview of when, where and for how long TTX was applied to *slc12a2b*^{ue58} mutants.
B. Confocal images of a Tg(mbp:EGFP-CAAX) control (top), *slc12a2b*^{ue58} mutant (middle) and *slc12a2b*^{ue58} mutant injected with TTX (bottom). Scale bar, 20 μm.
C. Quantitation of mean myelinated nerve diameter in controls, *slc12a2b*^{ue58} mutants and *slc12a2b*^{ue58} mutants injected with TTX. One-way ANOVA followed by Tukey's multiple comparison test was used to assess statistical significance. ****p<0.0001. Each point represents an individual animal.
D. Schematic overview of when, where and for how long TTX was applied to either constitutive or glial-specific *slc12a2b* mutants.
E. Confocal images of 6dpf *slc12a2b*^{ue58} mutant larvae. Top and bottom panels show the same region of the pLLn before and 4-6 hours after injection with either a control solution (left), or TTX (right). Scale bar, 20 μm.
F. Confocal images of 6dpf Tg(mbp:EGFP-CAAX) larvae, in which *slc12a2b* has been targeted in myelinating glial cells. Top and bottom panels show the same region of the pLLn before and 4-6 hours after injection with either a control solution (left), or TTX (right). Scale bar, 20 μm.
G. Quantitation of the change in mean myelinated nerve diameter following injection with either a control solution or TTX in *slc12a2b* mutants (G) or animals in which *slc12a2b* has been disrupted specifically in myelinating glial cells (H). Two-tailed Student's t-test was used to assess statistical significance. ****p<0.0001. Each point represents an individual animal.

Our results raise the question as to how neuronal activity can trigger such a severe pathology in myelinated axons in the absence of either neuronal or Schwann cell NKCC1b. We predict that ions released into the periaxonal space upon action potential firing might not be appropriately buffered with impaired NKCC1b, and that this leads to a cascade of dysregulation that culminates in the severe pathology observed. Given that K^+ ions are released into the periaxonal space upon action potential firing, failure to buffer K^+ may be a key contributor to the observed pathology, but how NKCC1b loss of function leads to ion and solute imbalance causing the observed pathologies, and so rapidly, remains to be investigated. The severe pathology in the *slc12a2b*^{ue58} mutant PNS begs the question as to why CNS myelin is less severely affected. One possibility is that the second NKCC1-encoding gene in zebrafish, *slc12a2a,* can compensate for NKCC1b loss of function in the CNS, but not the PNS. Although we have not seen disruption to myelin in *slc12a2a* mutants (data not shown) the investigation of *slc12a2a, slc12a2b* double mutants will be required to test this. There is, however, only one NKCC1-encoding gene in mammals, and although mutant mice with conditional knockout of NKCC1 from the oligodendrocyte lineage show disrupted oligodendrocyte differentiation (Zonouzi et al., 2015), gross disruption to myelinated axon integrity was not reported. Therefore, an alternative explanation for the more severe effects of NKCC1b loss in the PNS compared to CNS may be the presence of factors with redundant functions in the CNS. For example, the inward rectifying potassium channel Kir4.1 has been proposed to regulate ion homeostasis at the axon-myelin interface in the CNS (Larson et al., 2018; Schirmer et al., 2018), and so it would be interesting to test whether Kir4.1 and NKCC1 have redundant or distinct roles in maintaining myelinated axon integrity.

As we noted earlier, the physiology of myelinated axons and in particular those related to the functional interactions at the axon-myelin interface and periaxonal space are only beginning to be elucidated. At present, there is increasing focus on the importance of this domain in the CNS, but our work indicates that the axon-myelin interface represents a domain of key importance to peripheral nerves as well. Indeed, Schwann cells express numerous neurotransmitter receptors (Christensen et al., 2016; Chen et al., 2017), as well as, ion channels and transporters (Baker, 2002). However, we have much to learn about which

factors are actually localised to the axon-myelin interface along myelinated peripheral axons in vivo. Indeed, our understanding of the interactions at the axon-myelin interface in the PNS and CNS remains an important area of investigation to help fully elucidate myelinated axon formation, health and function.

Materials and Methods

Zebrafish husbandry and transgenic lines

Adult zebrafish were housed and maintained in accordance with standard procedures in the Queen's Medical Research Institute zebrafish facility, University of Edinburgh. All experiments were performed in compliance with the UK Home Office, according to its regulations under project licenses 60/4035 and 70/8436. Adult zebrafish were subject to a 14/10 hr, light/dark cycle. Embryos were produced by pairwise matings and raised at 28.5˚C in 10 mM HEPES-buffered E3 Embryo medium or conditioned aquarium water with methylene blue. Embryos were staged according to days post-fertilisation (dpf). The following lines were used in this study: Tg(mbp:EGFP-CAAX) (Almeida et al., 2011), Tg(cntn1b:mCherry) (Czopka et al., 2013), Tg(claudinK:Gal4) (Münzel et al., 2012). The *ue58* allele was identified due to its striking disruption of mbp:EGFP-CAAX along the posterior lateral line nerve during the ENU-based forward genetic screen, underpinning this study, described in (Kegel et al., 2019; Klingseisen et al., 2019).

Identification of genetic linkage and causative mutation

Following an outcross to WIK, pooled DNA from 116 *ue58* mutant recombinants was sequenced on an Illumina HiSeq4000 (Edinburgh Genomics). We processed this data through a modified version of the Variant Discovery Mapping (VDM) CloudMap pipeline (Minevich et al., 2012), on an in-house Galaxy server using the Zv9/danRer7 genome and annotation. For both the VDM plots and assessing the list of candidate variants we subtracted a list of wildtype variants compiled from sequencing of the *ekwill* strain plus previously published data (Butler et al., 2015; LaFave et al., 2014; Obholzer et al., 2012).

From the prospective candidate mutations in the region of chromosome 8 linked to the mutant phenotype, we filtered for prospective nonsense mutations likely to result in strong loss of function of encoded proteins. The candidate list was further filtered by excluding polymorphisms found in other species or other mutants that we sequenced that derived from the ENU screen. We designed genotyping assays and identified only one candidate STOP codon inducing mutation that was linked to the *ue58* mutant phenotype. This mutation resided in CABZ01084010.1 on chromosome 8 (Zv9) and was unique in all *ue58* sequence reads. From then on, to genotype *ue58* mutant animals, *ue58/+* heterozygotes and wildtypes, we amplified DNA surrounding the location of the mutation using the following primers: 5' – TGATGTTTGTGTTTGTTTGGTCTCA-3' and 5'-CGCTCTGATGGTTTCCTCGG-3'.

The 145 bp wildtype PCR product is digested with MscI into 43 bp and 102 bp fragments, while mutant sequence remains uncut. Products were separated on a 2% agarose gel.

Amplification of NKCC1-encoding ORF

Using the Basic Local Alignment Search Tool (BLAST), we found alignment of sequence in the region of our candidate mutation with a separate, previously identified zebrafish gene, *slc12a2*, which encodes the solute transporter NKCC1.

To test whether a gene encoding a NKCC1-like product was encoded at this locus and to amplify full-length mRNA that might rescue the *ue58* mutant phenotype, we carried out PCR with high-fidelity DNA polymerase Q5 (NEB) from a pool of wildtype zebrafish total cDNA (reverse-transcribed from total mRNA extracted from AB 5 dpf zebrafish). We used forward primer 5'-CATCATGTCAGACCAGCCT-3' (underlined bases denote start predicted codon) and reverse primer 5'-CAGGAGTAGAAGGTCAGAAC-3' (underlined bases denote first two bases of

predicted stop codon), designed based on the partial transcript sequences available for each terminus of a possible *slc12a2b* gene. This PCR amplified a cDNA product of around 3.2 kb, which we purified and TOPO-cloned (using the Zero Blunt™ TOPO™ PCR Cloning Kit, ThermoFisher Scientific) to generate pCRII-slc12a2b. We sequenced four pCRII-slc12a2b clones and in all we identified a complete ORF of 3276bp. The termini-encoding regions of the ORF aligned well with the partial sequences in the database, and single-nucleotide variations were all annotated in SNPfisher (Butler et al., 2015) and similar between the clones, suggesting that these are true SNPs rather than mistakes introduced by the polymerase during PCR amplification. The *slc12a2b* cDNA was then subcloned into the pCS2+ vector for mRNA synthesis by digesting from pCRII-slc12a2b using EcoRI and ligating into EcoRI-digested and CIP-dephosphorylated pCS2+ vector. The *slc12a2b* cDNA sequence is available under Accession number MK648423.

For *slc12a2b*^{ue58} mRNA rescue experiments, progeny from homozygous Tg(mbp:EGFP-CAAX), *slc12a2b*^{ue58} parents were injected with 160 pg synthetic *slc12a2b*^{ue58} mRNA at the one-cell-stage and imaged at 4dpf for quantification of mean myelinated nerve diameter compared to Tg(mbp:EGFP-CAAX) wildtype controls and *slc12a2b*^{ue58} constitutive mutants.

CRISPR-Cas9 based targeting of *slc12a2b*

To independently disrupt *slc12a2b* function, we used IDT's CRISPR design tool to identify guide RNAs targeting sequences located in the putative exon 1 and putative exon 26 of the gene with predicted low off-target activity (exon 1: GGGAACCCGAGCCAGGCGG and exon 26: GGTGGACACCGTCCCCTTTC). Cas9 protein (New England Biolabs; 1 µg/µl final concentration) and sgRNA (18 ng/µl final concentration) were mixed in Cas9 nuclease reaction buffer (NEB; 20 mM HEPES, 100 mM NaCl, 5 mM $MgCl_2$, 0.1 mM EDTA, pH 6.5) containing 0.05% phenol red and incubated at 37°C for 10 mins. Approximately 2-3 nl of active sgRNA-Cas9 ribonucleoprotein complex was injected into Tg(mbp:EGFP-CAAX) embryos at the one-cell stage and myelin morphology assessed in the days following injection. For each sgRNA, at least two independent injection experiments were performed.

To genotype *slc12a2b*^{ue78} homozygous mutant animals, *slc12a2b*^{ue78}*/+* heterozygotes and wildtypes, we amplified DNA surrounding the location of the mutation in exon 1 using the following primers: 5' –GAAGTTCACCACACGGGACC-3' and 5'-GACAATACCGGGCGGTGTCC -3'. The 262 bp wildtype PCR product is digested with MwoI into 115 bp and 147 bp fragments, while the mutant sequence remains uncut. Products were separated on a 2% agarose gel.

Transmission Electron Microscopy

Control and *slc12a2b*^{ue58} mutant animals were prepared at 4-5 dpf by high-pressure freezing using a Leica EM ICE apparatus (Leica Microsystems, Vienna, Austria). As filler a solution of 20% PVP in E3 Embryo medium was used. Freeze substitution was performed as described (Weil et al., 2019). Epon embedded animals were cut with a 35° diamond knife (Diatome, Biel, Switzerland) using a UC7 ultramicrotome (Leica). Images were obtained with a LEO912 transmission electron microscope (Carl Zeiss Microscopy, Oberkochen, Germany) equipped with a 2k on-axis CCD camera (TRS, Moorenweis, Germany).

Single cell labelling

To mosaically label individual Schwann cells, we injected one-cell stage Tg(claudinK:Gal4) embryos with a 1 nl solution containing 10 ng/µl pTol2-UAS:EGFP-pA or pTol2-UAS:memScarlet-pA to label the cytoplasm or membrane of control cells respectively along with 25 ng/µl *tol2* transposase mRNA. To generate Schwann cells with disrupted *slc12a2b* function, we additionally injected embryos with CRISPR sgRNA targeting exon 1 of the *slc12a2b* gene.

Cell-type specific targeting of *slc12a2b* in neurons and myelinating glial cells

To disrupt *slc12a2b* function specifically in neurons or myelinating glial cells, we cloned the *slc12a2b* guide sequence targeting exon 1 that had shown high mutation efficiency into a Tol2 modular vector system that allows co-expression of Cas9 under a tissue-specific promoter (Ablain et al., 2015). Oligonucleotides encoding the 20 bp *slc12a2b* exon 1 guide sequence were purchased from Integrated DNA Technologies (IDT) and ligated into the pDestTol2CG2-U6:gRNA destination vector (63156 Addgene) following BseRI (NEB) restriction digest under the zebrafish U6-3 promoter. This vector also contains GFP under the heart-specific *cmlc2* promoter as a marker of transgenesis. To enable neuron or glial-specific *slc12a2b* loss-of-function, we then performed Gateway reactions with 5' entry vectors containing either a 5 kb genomic fragment of zebrafish Neurofilament medium polypeptide a (Nefma) regulatory sequence (see below) or a 6 kb fragment of neural-specific beta tubulin (NBT) or a 2 kb genomic fragment of zebrafish genomic *mbp* regulatory sequence (Almeida et al., 2011), with a middle entry vector containing membrane-bound tagRFPt, followed by the self-cleaving T2A peptide and zebrafish codon-optimised Cas9 sequence flanked by two nuclear localisation signals and 3' entry vector containing a polyA sequence (#302 from Tol2Kit) (Kwan et al., 2007) (**Figure 3A**).

One-cell stage zebrafish embryos were injected with 1 nl of a solution containing 10 ng/µl plasmid DNA, 25 ng/µl transposase mRNA and 0.05% phenol red. Embryos were screened at 3 dpf for transgene integration as indicated by green heart expression.

Cloning of the Nefma regulatory sequence

We amplified 5 kb of sequence immediately upstream of the nefma gene ORF (NM_001111214.2) from wildtype genomic zebrafish DNA using the following primers, which also included attB1 and attB2R sequences (underlined) for cloning purposes:

Fwd Primer – GGGGACAACTTTGTATAGAAAAGTTGCCACCGTAATTAACAAATATCCATCAC

Rev Primer - GGGGACTGCTTTTTTGTACAAACTTGCGAACTGACGGGGAGTGGAGGTG

The resulting PCR fragment was cloned into the pDONRP4-P1R plasmid to use as a p5E vector for gateway cloning.

Pharmacological treatments

To inhibit neuronal electrical activity, we injected a 2 nL volume of 0.5 mM tetrodotoxin (TTX) (Tocris Bioscience) into the yolk of zebrafish larvae. A 3 mM stock of TTX, dissolved in water, was diluted in 10 mM HEPES-buffered E3 Embryo medium (pH adjusted 7.4) containing 0.05% phenol red for injection. Control larvae were injected with a vehicle solution of E3 Embryo medium containing 0.05% phenol red. For prevention experiments, 3 dpf larvae homozygous for *slc12a2b*^{ue58}; Tg(mbp:EGFP-CAAX) or Tg(mbp:EGFP-CAAX) as control were used. For rescue experiments, either larvae homozygous for *slc12a2b*^{ue58}; Tg(mbp:EGFP-CAAX) or one-cell stage Tg(mbp:EGFP-CAAX) embryos injected with the construct mbp:memtagRFPt2Acas9;

U6:Slc12a2b to enable glial-specific disruption of the gene *slc12a2b* were used. Larvae exhibiting signs of myelin pathology were imaged at 6 dpf and subsequently injected with TTX or a control solution followed by repeat imaging of the same region of the posterior later line (around the level of somite 6 for *slc12a2b*^{ue58} mutants) 4-6 hours later. The efficiency of injections was assessed by complete paralysis of larvae that persisted until the point of imaging. General health of injected larvae was assessed prior to imaging and any larva showing signs of overt ill-health excluded from imaging and analysis.

Live imaging and image analysis

Live imaging of all transgenic reporters was carried out on a Zeiss 880 LSM with Airyscan FAST, typically in super-resolution mode, using a 20X objective lens (NA=0.8). An Olympus microscope capable of differential interference contrast imaging was used to image tissue oedema in *slc12a2b*^{ue58} mutants using a 60X water-immersion objective lens (NA=1). A Nomarski prism and polarizer were oriented in such a way as to provide Differential Interference Contrast (DIC). All images depict a lateral view of the spinal cord with anterior to the left and dorsal to the top. Figure panels were prepared using Fiji and Adobe Illustrator CS6.

To quantify myelin morphology from images of live Tg(mbp:EGFP-CAAX) animals we carried out automatic thresholding of maximum intensity projections, via the Huang method using ImageJ/FIJI (Schindelin et al., 2015; 2012). The thresholded images were then converted to masks, inverted, and objects detected using ImageJ's Analyse Particles function. Identified particles were then assessed for area (μm^2) and relative fluorescence intensity (mean grey value), and total fluorescence calculated as the sum of (mean grey value*particle area) for all relevant particles in any given image. The total visible myelinated nerve length was calculated (by summing all X-coordinates uniquely occupied by particles), and used to calculate either the mean myelinated nerve or Schwann cell diameter (total area/visible myelinated nerve length).

Statistical analysis

Statistical tests were carried out using GraphPad Prism (version 8). Data was tested for normal distribution using D'Agostino-Pearson omnibus test and tested for significance by two-tailed Student's t-test or one-way analysis of variance (ANOVA) with Tukey's multiple comparisons test where applicable. All data are expressed as mean ± SD. All data points represent individual animals unless otherwise specified as indicated in the figure legends, with symbols indicating the following p value ranges: *$p < 0.05$, **$p < 0.01$, *** $p < 0.001$, **** $p < 0.0001$.

Supplementary Information

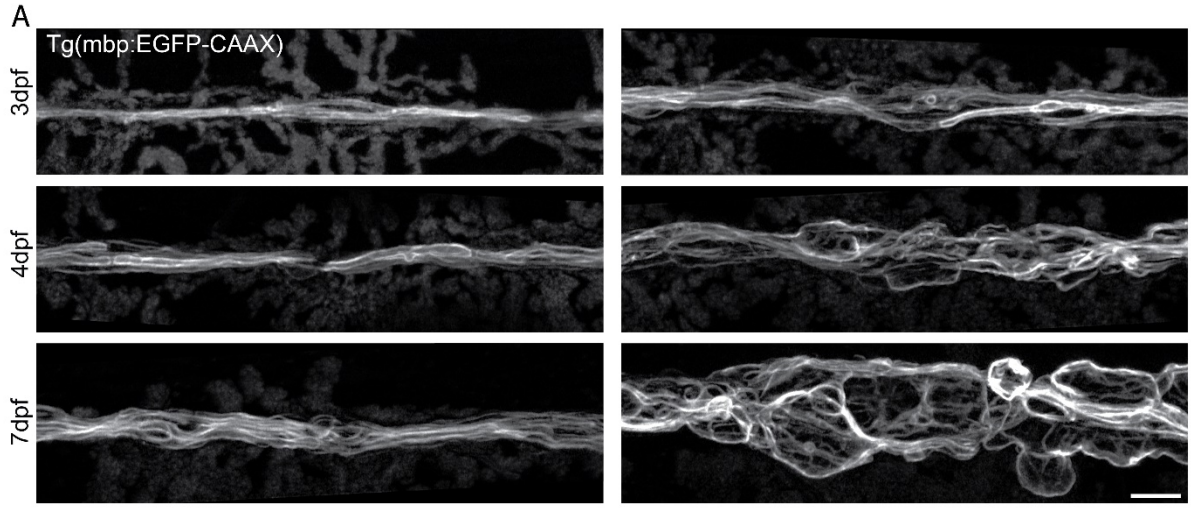

Supplementary Figure 1. Myelin in *ue58* mutants forms normally but becomes progressively disrupted.
A. Confocal images of Tg(mbp:EGFP-CAAX) heterozygote (left) and *ue58* homozygote mutant (right) at 3dpf, 4dpf and 7dpf. Scale bar= 10 µm.

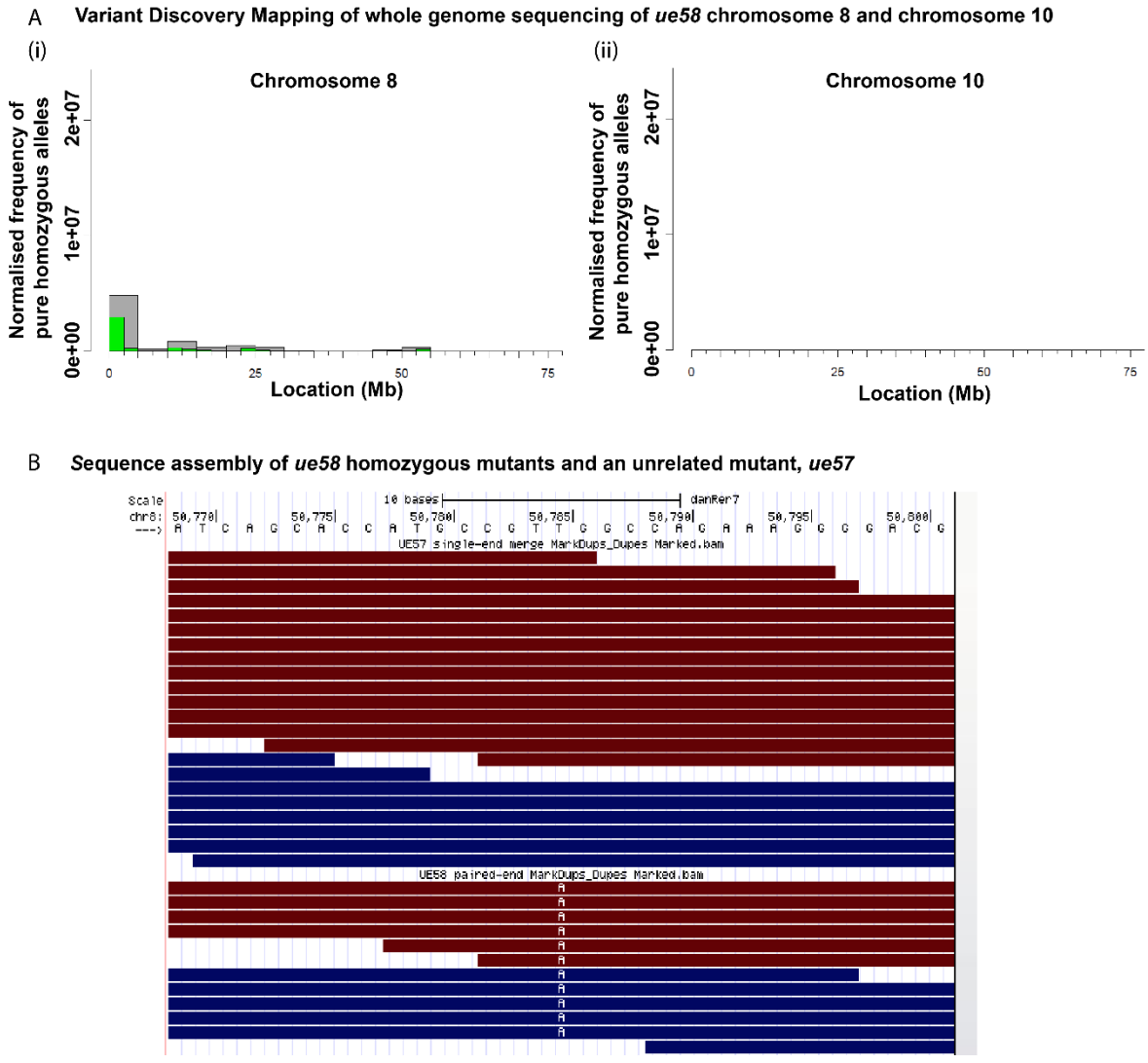

Supplementary Figure 2. Molecular characterization of the *ue58* mutation and *slc12a2b*.
A. Variant discovery mapping plots from the CloudMap pipeline showing the normalized frequency of pure homozygous variants (allele frequency in recombinant pool = 1.0) in 2.5 Mb (green) or 5 Mb (grey) bins. Note linkage at the beginning of Chromosome 8, but none in 10, as a comparison, and where *slc12a2a* is localised.
B. Raw sequence reads in the candidate region defined by mapping shows a T to A change in the *ue58* mutant reads, but not in an unrelated mutant, *ue57*.

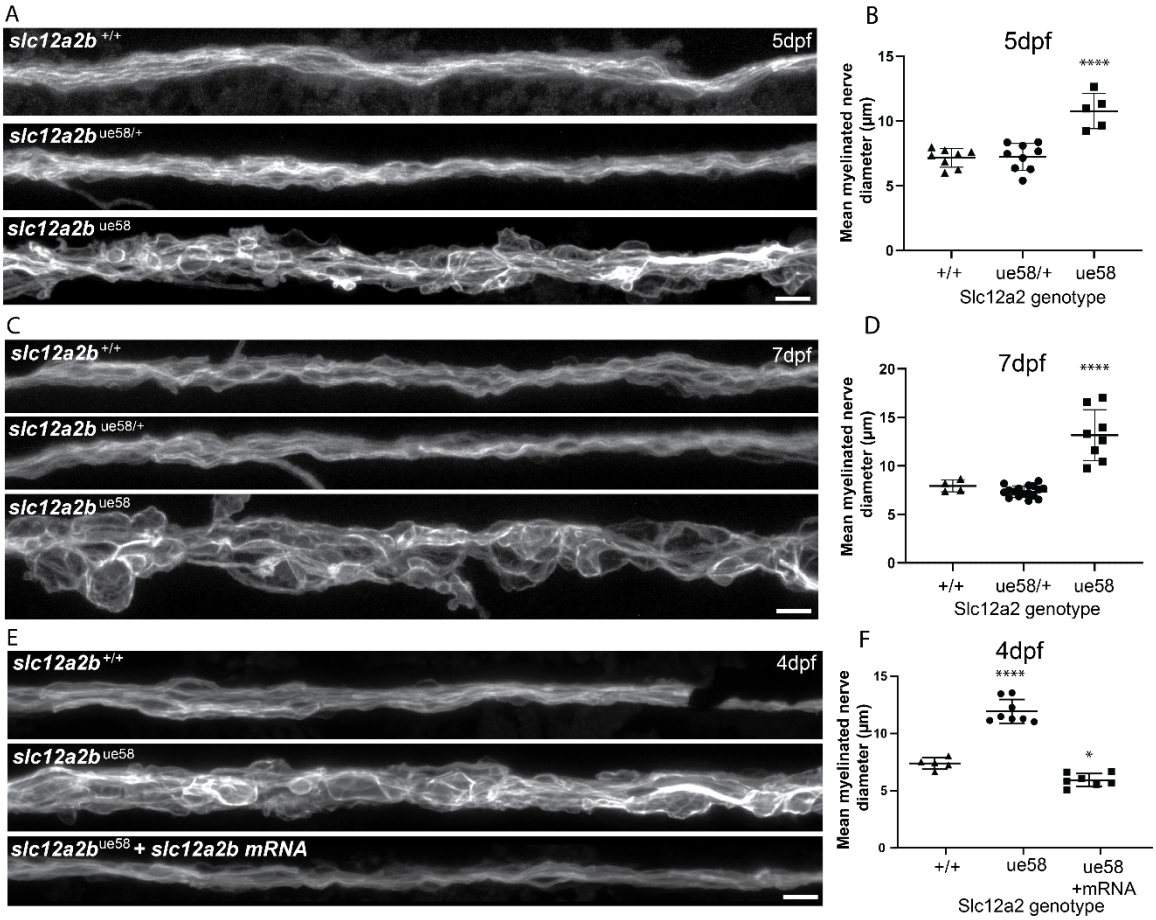

Supplementary Figure 3. Disruption to *slc12a2b* leads to myelin pathology.

A. Images of Tg(mbp:EGFP-CAAX) wildtype, *slc12a2b* $^{ue58/+}$ and *slc12a2b* mutant animals at 5dpf. Scale bar, 10 μm.

B. Quantitation of mean myelinated nerve diameter in wildtype, *slc12a2b* $^{ue58/+}$ and *slc12a2b* mutant animals at 5dpf. One-way ANOVA followed by Tukey's multiple comparison test was used to assess statistical significance. Each point represents an individual animal.

C. Images of Tg(mbp:EGFP-CAAX) wildtype, *slc12a2b* $^{ue58/+}$ and *slc12a2b* mutant animals at 7dpf. Scale bar, 10 μm.

D. Quantitation of mean myelinated nerve diameter in wildtype, *slc12a2b* $^{ue58/+}$ and *slc12a2b* mutant animals at 7dpf. One-way ANOVA followed by Tukey's multiple comparison test was used to assess statistical significance. Each point represents an individual animal.

E. Images of Tg(mbp:EGFP-CAAX) wildtype, control injected *slc12a2b* mutant and *slc12a2b* mRNA injected mutant animals at 4dpf. Scale bar, 10 μm.

F. Quantitation of mean myelinated nerve diameter in wildtype, control injected *slc12a2b* mutant and *slc12a2b* mRNA injected mutant animals at 4dpf. One-way ANOVA followed by Tukey's multiple comparison test was used to assess statistical significance. *p<0.05, ****p<0.0001. Each point represents an individual animal.

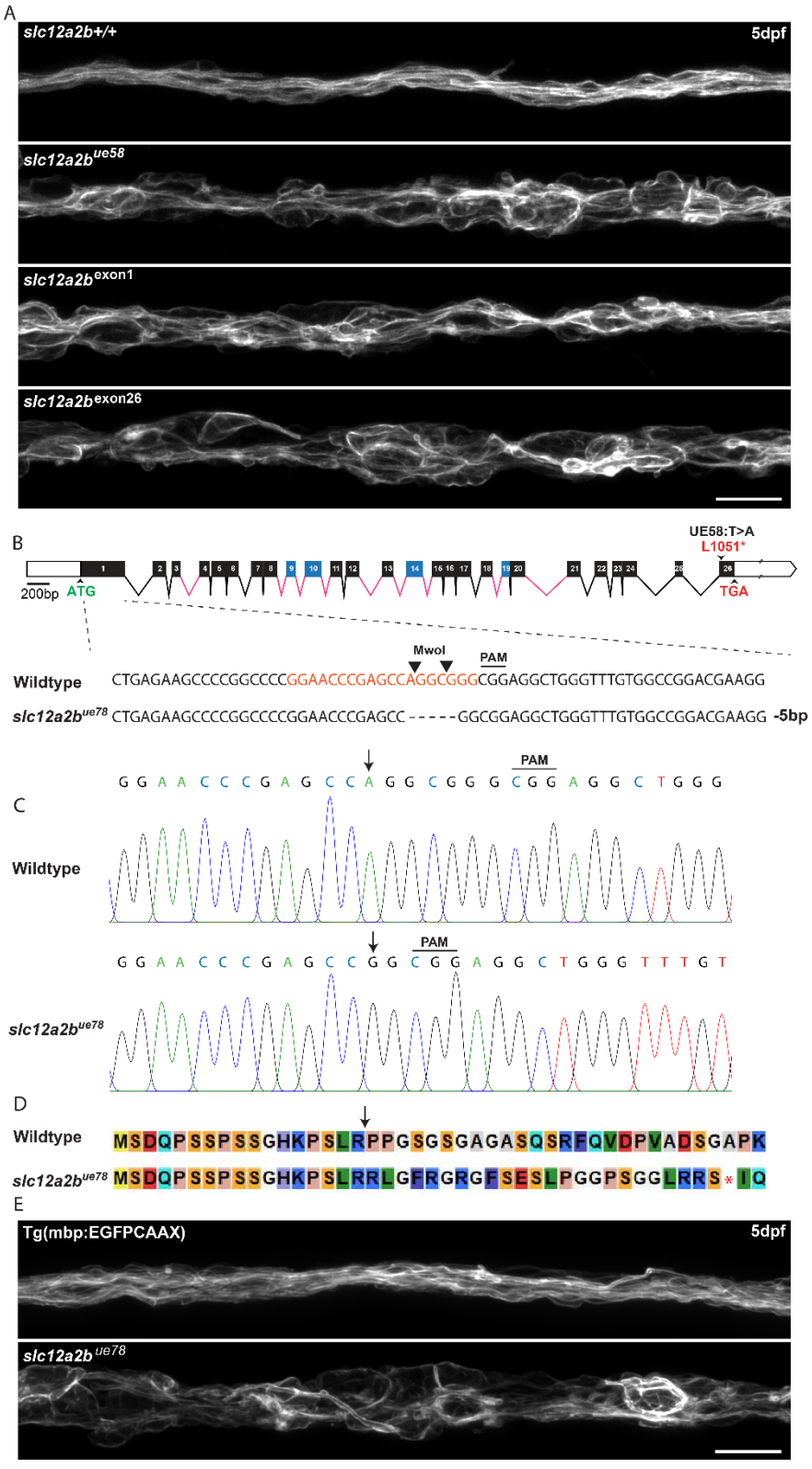

Supplementary Figure 4. Validation of *slc12a2b* loss of function in CRISPR/Cas9 mutant animals.
A. Images of Tg(mbp:EGFP-CAAX) wildtype (top), *slc12a2b* mutant animals (2nd panel) and Tg(mbp:EGFP-CAAX) wildtype animals injected with CRISPR guide RNAs targeting exon 1 of *slc12a2b* (3rd panel) and exon 26 (bottom panel) of *slc12a2b*. Scale bar, 20 μm.
B. Genomic structure of the zebrafish *slc12a2b* gene, as in figure 1, showing the CRISPR guide RNA targeting sequence located within exon 1 (orange). Sanger sequencing from second generation *slc12a2b*^{ue78} mutants reveals a 5 bp deletion upstream of the PAM cleavage site within exon 1 of the *slc12a2b* gene. Deletion of this

sequence disrupts the MwoI restriction enzyme recognition site allowing mutant animals to be genotyped based on the presence of undigested product.
C. Sanger sequence chromatograms of *slc12a2b*^{ue78} mutants compared to wildtype controls showing region of 5 bp deletion (arrows).
D. Alignment of predicted amino acid sequences in *slc12a2b*^{ue78} mutants and wildtype controls. The 5 bp deletion in mutants produces a frameshift in the coding sequence (arrow) and introduction of a premature translational stop codon (asterisk).
E. Confocal images of 5dpf Tg(mbp:EGFP-CAAX) wildtype (top) and second generation *slc12a2b*^{ue78} mutant animals (bottom) showing major myelin disruption along the pLLn. Scale bar, 20 μm.

Supplementary Figure 5. Periaxonal space swelling, axonal enlargement and myelin outfoldings in *slc12a2b*^{ue58} mutants.
A. TEM images of control (left) and *slc12a2b*^{ue58} mutant animals (middle and right) showing an enlarged axon (asterisk) and periaxonal swelling, and myelin outfoldings (arrowheads). Scale bar, 1 μm.

References

Abbas, L., and T.T. Whitfield. 2009. Nkcc1 (Slc12a2) is required for the regulation of endolymph volume in the otic vesicle and swim bladder volume in the zebrafish larva. *Development*. 136:2837–2848. doi:10.1242/dev.034215.

Ablain, J., E.M. Durand, S. Yang, Y. Zhou, and L.I. Zon. 2015. A CRISPR/Cas9 vector system for tissue-specific gene disruption in zebrafish. *Developmental Cell*. 32:756–764. doi:10.1016/j.devcel.2015.01.032.

Almeida, R.G., and D.A. Lyons. 2017. On Myelinated Axon Plasticity and Neuronal Circuit Formation and Function. *J. Neurosci.* 37:10023–10034. doi:10.1523/JNEUROSCI.3185-16.2017.

Almeida, R.G., T. Czopka, C. ffrench-Constant, and D.A. Lyons. 2011. Individual axons regulate the myelinating potential of single oligodendrocytes in vivo. *Development*. 138:4443–4450. doi:10.1242/dev.071001.

Baker, M.D. 2002. Electrophysiology of mammalian Schwann cells. *Prog. Biophys. Mol. Biol.* 78:83–103.

Ben-Ari, Y. 2017. NKCC1 Chloride Importer Antagonists Attenuate Many Neurological and Psychiatric Disorders. *Trends in Neurosciences*. 40:536–554. doi:10.1016/j.tins.2017.07.001.

Blaesse, P., M.S. Airaksinen, C. Rivera, and K. Kaila. 2009. Cation-Chloride Cotransporters and Neuronal Function. *Neuron*. 61:820–838. doi:10.1016/j.neuron.2009.03.003.

Butler, M.G., J.R. Iben, K.C. Marsden, J.A. Epstein, M. Granato, and B.M. Weinstein. 2015. SNPfisher: tools for probing genetic variation in laboratory-reared zebrafish. *Development*. 142:1542–1552. doi:10.1242/dev.118786.

Chen, T.-J., N. Fröhlich, B. Kula, R. Barzan, and M. Kukley. 2017. Glutamate Activates AMPA Receptor Conductance in the Developing Schwann Cells of the Mammalian Peripheral Nerves. *J. Neurosci.* 37:11818–11834. doi:10.1523/JNEUROSCI.1168-17.2017.

Chew, T.A., B.J. Orlando, J. Zhang, N.R. Latorraca, A. Wang, S.A. Hollingsworth, D.-H. Chen, R.O. Dror, M. Liao, and L. Feng. 2019. Structure and mechanism of the cation-chloride cotransporter NKCC1. *Nature*. 572:488–492. doi:10.1038/s41586-019-1438-2.

Christensen, P.C., N.C. Welch, C. Brideau, and P.K. Stys. 2016. Functional ionotropic glutamate receptors on peripheral axons and myelin. *Muscle Nerve*. 54:451–459. doi:10.1002/mus.25078.

Cohen, C.C.H., M.A. Popovic, J. Klooster, M.-T. Weil, W. Möbius, K.-A. Nave, and M.H.P. Kole. 2020. Saltatory Conduction along Myelinated Axons Involves a Periaxonal Nanocircuit. *Cell*. 1–28. doi:10.1016/j.cell.2019.11.039.

Czopka, T., C. ffrench-Constant, and D.A. Lyons. 2013. Individual oligodendrocytes have only

a few hours in which to generate new myelin sheaths in vivo. *Developmental Cell*. 25:599–609. doi:10.1016/j.devcel.2013.05.013.

Delpire, E., J. Lu, R. England, C. Dull, and T. Thorne. 1999. Deafness and imbalance associated with inactivation of the secretory Na-K-2Cl co-transporter. *Nat. Genet.* 22:192–195. doi:10.1038/9713.

Dixon, M.J., J. Gazzard, S.S. Chaudhry, N. Sampson, B.A. Schulte, and K.P. Steel. 1999. Mutation of the Na-K-Cl co-transporter gene Slc12a2 results in deafness in mice. *Human molecular genetics*. 8:1579–1584. doi:10.1093/hmg/8.8.1579.

Fields, R.D. 2015. A new mechanism ofnervous system plasticity: activity-dependent myelination. *Nat Rev Neurosci*. 16:756–767. doi:10.1038/nrn4023.

Flagella, M., L.L. Clarke, M.L. Miller, L.C. Erway, R.A. Giannella, A. Andringa, L.R. Gawenis, J. Kramer, J.J. Duffy, T. Doetschman, J.N. Lorenz, E.N. Yamoah, E.L. Cardell, and G.E. Shull. 1999. Mice lacking the basolateral Na-K-2Cl cotransporter have impaired epithelial chloride secretion and are profoundly deaf. *The Journal of biological chemistry*. 274:26946–26955.

Fünfschilling, U., L.M. Supplie, D. Mahad, S. Boretius, A.S. Saab, J. Edgar, B.G. Brinkmann, C.M. Kassmann, I.D. Tzvetanova, W. Möbius, F. Diaz, D. Meijer, U. Suter, B. Hamprecht, M.W. Sereda, C.T. Moraes, J. Frahm, S. Goebbels, and K.-A. Nave. 2012. Glycolytic oligodendrocytes maintain myelin and long-term axonal integrity. *Nature*. 485:517–521. doi:10.1038/nature11007.

Gagnon, K.B., and E. Delpire. 2013. Physiology of SLC12 transporters: lessons from inherited human genetic mutations and genetically engineered mouse knockouts. *Am. J. Physiol., Cell Physiol.* 304:C693–714. doi:10.1152/ajpcell.00350.2012.

Gibson, E.M., A.C. Geraghty, and M. Monje. 2018. Bad wrap: Myelin and myelin plasticity in health and disease. *Dev Neurobiol*. 78:123–135. doi:10.1002/dneu.22541.

Jha, M.K., Y. Lee, K.A. Russell, F. Yang, R.M. Dastgheyb, P. Deme, X.H. Ament, W. Chen, Y. Liu, Y. Guan, M.J. Polydefkis, A. Höke, N.J. Haughey, J.D. Rothstein, and B.M. Morrison. 2019. Monocarboxylate transporter 1 in Schwann cells contributes to maintenance of sensory nerve myelination during aging. *Glia*. 68:161–177. doi:10.1002/glia.23710.

Kegel, L., M. Rubio, R.G. Almeida, S. Benito, A. Klingseisen, and D.A. Lyons. 2019. Forward Genetic Screen Using Zebrafish to Identify New Genes Involved in Myelination. *Methods in molecular biology (Clifton, N.J*. 1936:185–209. doi:10.1007/978-1-4939-9072-6_11.

Klingseisen, A., A.-M. Ristoiu, L. Kegel, D.L. Sherman, M. Rubio-Brotons, R.G. Almeida, S. Koudelka, S.K. Benito-Kwiecinski, R.J. Poole, P.J. Brophy, and D.A. Lyons. 2019. Oligodendrocyte Neurofascin Independently Regulates Both Myelin Targeting and Sheath Growth in the CNS. *Developmental Cell*. 51:730–744.e6. doi:10.1016/j.devcel.2019.10.016.

Kwan, K.M., E. Fujimoto, C. Grabher, B.D. Mangum, M.E. Hardy, D.S. Campbell, J.M. Parant,

H.J. Yost, J.P. Kanki, and C.B. Chien. 2007. The Tol2kit: a multisite gateway-based construction kit for Tol2 transposon transgenesis constructs. *Dev. Dyn.* 236:3088–3099.

LaFave, M.C., G.K. Varshney, M. Vemulapalli, J.C. Mullikin, and S.M. Burgess. 2014. A defined zebrafish line for high-throughput genetics and genomics: NHGRI-1. *Genetics*. 198:167–170. doi:10.1534/genetics.114.166769.

Larsen, B.R., M. Assentoft, M.L. Cotrina, S.Z. Hua, M. Nedergaard, K. Kaila, J. Voipio, and N. MacAulay. 2014. Contributions of the Na^+/K^+-ATPase, NKCC1, and Kir4.1 to hippocampal K^+ clearance and volume responses. *Glia*. 62:608–622. doi:10.1002/glia.22629.

Larson, V.A., Y. Mironova, K.G. Vanderpool, A. Waisman, J.E. Rash, A. Agarwal, and D.E. Bergles. 2018. Oligodendrocytes control potassium accumulation in white matter and seizure susceptibility. *Elife*. 7:e34829. doi:10.7554/eLife.34829.

Lee, Y., B.M. Morrison, Y. Li, S. Lengacher, M.H. Farah, P.N. Hoffman, Y. Liu, A. Tsingalia, L. Jin, P.-W. Zhang, L. Pellerin, P.J. Magistretti, and J.D. Rothstein. 2012. Oligodendroglia metabolically support axons and contribute to neurodegeneration. *Nature*. 487:443–448. doi:10.1038/nature11314.

Leiserson, W.M., B. Forbush, and H. Keshishian. 2010. Drosophila glia use a conserved cotransporter mechanism to regulate extracellular volume. *Glia*. 59:320–332. doi:10.1002/glia.21103.

MacAulay, N., and T. Zeuthen. 2010. Water transport between CNS compartments: Contributions of aquaporins and cotransporters. *Neuroscience*. 168:941–956. doi:10.1016/j.neuroscience.2009.09.016.

Macvicar, B.A., D. Feighan, A. Brown, and B. Ransom. 2001. Intrinsic optical signals in the rat optic nerve: Role for K+ uptake via NKCC1 and swelling of astrocytes. *Glia*. 37:114–123. doi:10.1002/glia.10023.

Micu, I., J.R. Plemel, A.V. Caprariello, K.-A. Nave, and P.K. Stys. 2018. Axo-myelinic neurotransmission: a novel mode of cell signalling in the central nervous system. *Nat Rev Neurosci*. 19:49–58. doi:10.1038/nrn.2017.128.

Micu, I., J.R. Plemel, C. Lachance, J. Proft, A.J. Jansen, K. Cummins, J. van Minnen, and P.K. Stys. 2016. Experimental Neurology. *Experimental Neurology*. 276:41–50. doi:10.1016/j.expneurol.2015.10.006.

Minevich, G., D.S. Park, D. Blankenberg, R.J. Poole, and O. Hobert. 2012. CloudMap: A Cloud-Based Pipeline for Analysis of Mutant Genome Sequences. *Genetics*. 192:1249–1269. doi:10.1534/genetics.112.144204.

Monje, M. 2018. Myelin Plasticity and Nervous System Function. *Annual review of neuroscience*. 41:61–76. doi:10.1146/annurev-neuro-080317-061853.

Moyon, S., R. Frawley, K.L. Marshall-Phelps, L. Kegel, S.M. Bostrand, B. Sadowski, D. Huang, Y.-H. Jiang, D. lyons, W. Möbius, and P. Casaccia. 2019. TET1-mediated DNA hydroxy-

methylation regulates adult remyelination. *bioRxiv*. 62:908. doi:10.1101/819995.

Münzel, E.J., K. Schaefer, B. Obirei, E. Kremmer, E.A. Burton, V. Kuscha, C.G. Becker, C. Brösamle, A. Williams, and T. Becker. 2012. Claudin k is specifically expressed in cells that form myelin during development of the nervous system and regeneration of the optic nerve in adult zebrafish. *Glia*. 60:253–270. doi:10.1002/glia.21260.

Obholzer, N., I.A. Swinburne, E. Schwab, A.V. Nechiporuk, T. Nicolson, and S.G. Megason. 2012. Rapid positional cloning of zebrafish mutations by linkage and homozygosity mapping using whole-genome sequencing. *Development*. 139:4280–4290. doi:10.1242/dev.083931.

Rash, J.E., K.G. Vanderpool, T. Yasumura, J. Hickman, J.T. Beatty, and J.I. Nagy. 2016. KV1 channels identified in rodent myelinated axons, linked to Cx29 in innermost myelin: support for electrically active myelin in mammalian saltatory conduction. *Journal of Neurophysiology*. 115:1836–1859. doi:10.1152/jn.01077.2015.

Saab, A.S., I.D. Tzvetavona, A. Trevisiol, S. Baltan, P. Dibaj, K. Kusch, W. Möbius, B. Goetze, H.M. Jahn, W. Huang, H. Steffens, E.D. Schomburg, A. Pérez-Samartín, F. Pérez-Cerdá, D. Bakhtiari, C. Matute, S. Löwel, C. Griesinger, J. Hirrlinger, F. Kirchhoff, and K.-A. Nave. 2016. Oligodendroglial NMDA Receptors Regulate Glucose Import and Axonal Energy Metabolism. *Neuron*. 91:119–132. doi:10.1016/j.neuron.2016.05.016.

Schindelin, J., C.T. Rueden, M.C. Hiner, and K.W. Eliceiri. 2015. The ImageJ ecosystem: An open platform for biomedical image analysis. *Mol. Reprod. Dev.* 82:518–529. doi:10.1002/mrd.22489.

Schindelin, J., I. Arganda-Carreras, E. Frise, V. Kaynig, M. Longair, T. Pietzsch, S. Preibisch, C. Rueden, S. Saalfeld, B. Schmid, J.-Y. Tinevez, D.J. White, V. Hartenstein, K. Eliceiri, P. Tomancak, and A. Cardona. 2012. Fiji: an open-source platform for biological-image analysis. *Nat Meth*. 9:676–682. doi:10.1038/nmeth.2019.

Schirmer, L., W. Möbius, C. Zhao, A. Cruz-Herranz, L. Ben Haim, C. Cordano, L.R. Shiow, K.W. Kelley, B. Sadowski, G. Timmons, A.-K. Pröbstel, J.N. Wright, J.H. Sin, M. Devereux, D.E. Morrison, S.M. Chang, K. Sabeur, A.J. Green, K.-A. Nave, R.J. Franklin, and D.H. Rowitch. 2018. Oligodendrocyte-encoded Kir4.1 function is required for axonal integrity. *Elife*. 7:651. doi:10.7554/eLife.36428.

Stassart, R.M., W. Möbius, K.-A. Nave, and J.M. Edgar. 2018. The Axon-Myelin Unit in Development and Degenerative Disease. *Front Neurosci*. 12:274–22. doi:10.3389/fnins.2018.00467.

Stenesen, D., A.T. Moehlman, J.N. Schellinger, A.R. Rodan, and H. Krämer. 2019. The glial sodium-potassium-2-chloride cotransporter is required for synaptic transmission in the Drosophila visual system. *Sci Rep*. 9:2475–15. doi:10.1038/s41598-019-38850-x.

Su, G., D.B. Kintner, M. Flagella, G.E. Shull, and D. Sun. 2002. Astrocytes from Na +-K +-Cl −cotransporter-null mice exhibit absence of swelling and decrease in EAA release. *Am. J. Physiol., Cell Physiol.* 282:C1147–C1160. doi:10.1152/ajpcell.00538.2001.

Suminaite, D., D.A. Lyons, and M.R. Livesey. 2019. Myelinated axon physiology and regulation of neural circuit function. *Glia*. 185:181–13. doi:10.1002/glia.23665.

Wang, H., D.D. Kunkel, T.M. Martin, P.A. Schwartzkroin, and B.L. Tempel. 1993. Heteromultimeric K+ channels in terminal and juxtaparanodal regions of neurons. *Nature*. 365:75–79. doi:10.1038/365075a0.

Weil, M.-T., T. Ruhwedel, M. Meschkat, B. Sadowski, and W. Möbius. 2019. Transmission Electron Microscopy of Oligodendrocytes and Myelin. *Methods in molecular biology (Clifton, N.J*. 1936:343–375. doi:10.1007/978-1-4939-9072-6_20.

Yousuf, M.S., K. Zubkow, G. Tenorio, and B. Kerr. 2017. The chloride co-transporters, NKCC1 and KCC2, in experimental autoimmune encephalomyelitis (EAE). *Neuroscience*. 344:178–186. doi:10.1016/j.neuroscience.2016.12.046.

Zeuthen, T., and N. MacAulay. 2012. Cotransport of water by Na^+-K^+-$2Cl^-$ cotransporters expressed in Xenopus oocytes: NKCC1 versus NKCC2. *The Journal of Physiology*. 590:1139–1154. doi:10.1113/jphysiol.2011.226316.

Zonouzi, M., J. Scafidi, P. Li, B. McEllin, J. Edwards, J.L. Dupree, L. Harvey, D. Sun, C.A. Hübner, S.G. Cull-Candy, M. Farrant, and V. Gallo. 2015. GABAergic regulation of cerebellar NG2 cell development is altered in perinatal white matter injury. *Nat Neurosci*. 18:674–682. doi:10.1038/nn.3990.